Full paper

Monitoring multi-respiratory indices via a smart nanofibrous mask filter based on a triboelectric nanogenerator

Haijun He [a], Jian Guo [b], Balázs Illés [c], Attila Géczy [c], Balázs Istók [d], Viktor Hliva [a], Dániel Török [a], József Gábor Kovács [a,f], István Harmati [b], Kolos Molnár [a,e,*]

[a] Department of Polymer Engineering, Faculty of Mechanical Engineering, Budapest University of Technology and Economics, Műegyetem rkp. 3, H-1111 Budapest, Hungary
[b] Department of Control Engineering and Information Technology, Faculty of Electrical Engineering and Informatics, Budapest University of Technology and Economics, Műegyetem rkp. 3, H-1111 Budapest, Hungary
[c] Department of Electronics Technology, Faculty of Electrical Engineering and Informatics, Budapest University of Technology and Economics, Műegyetem rkp. 3, H-1111 Budapest, Hungary
[d] Department of Fluid Mechanics, Faculty of Mechanical Engineering, Budapest University of Technology and Economics, Műegyetem rkp. 3, H-1111 Budapest, Hungary
[e] MTA–BME Research Group for Composite Science and Technology, Műegyetem rkp. 3, H-1111 Budapest, Hungary
[f] MTA-BME Lendület Lightweight Polymer Composites Research Group, Műegyetem rkp. 3, H-1111 Budapest, Hungary

ARTICLE INFO

ABSTRACT

Respiratory parameters, such as respiratory rate (RR), inhalation time (t_{in}), exhalation time (t_{ex}), and their ratio ($IER=t_{in}/t_{ex}$), are of great importance to indicate clinical differences between healthy people and those with respiratory diseases. Herein, we report a respiration monitoring triboelectric nanogenerator (RM-TENG) with nanofibrous membranes, which can be used as a smart, changeable, self-powered mask filter with high filtration efficiency for monitoring multiple respiratory indices (e.g., RR, t_{in}, t_{ex}, IER). We created a mathematical model to quantitatively analyze the effects of gap distance between two triboelectric layers on the contact area by recording the nanofibers layer's deformation profile with digital image correlation (DIC) tests. The RM-TENG is more sensitive to smaller gap distances between 1 mm and 5 mm because the high specific area of nanofibers can provide a more effective contact area. An RM-TENG built with optimized structure parameters can accurately and consistently detect the above-mentioned respiratory indices with excellent sensing stability for 40 h. The monitored RR and IER have 100% and 93.53% agreement with the real-time RR and IER set on the ventilator, respectively. Furthermore, it has a filtration efficiency of 99 wt% for particle sizes between 0.3 μm and 5 μm. This study introduces a mask filter fabricated with a simple structure with both filtering and sensing capability, which has excellent potential for self-powered health diagnostics.

1. Introduction

With the outbreak of coronavirus disease in 2019 (COVID-19), governments have mandated wearing a face mask to stop virus transmission and protect the people [1]. Especially those infected with COVID-19 must wear a mask all the time, even in hospitals. Undoubtedly, it is important to develop a smart mask that can monitor the respiratory state of the infected patient in situ without the need to wear uncomfortable sensors, because breathing is an essential physiological process for living organisms, which is related to gas exchange through bringing in oxygen (inhalation) and flushing out carbon dioxide (exhalation). The process of

inhalation and exhalation is defined as a breathing cycle. Respiratory characteristics are vital signs used to indicate the progression of illness [2]. Respiratory rate is a more common parameter used to indicate health conditions than other parameters, such as pulse and blood pressure [3]. There are many devices for monitoring respiratory rate; they can be classified into contact and noncontact monitoring systems. Contact respiratory monitoring instruments have to directly contact the body of the wearer to detect the respiratory sound [4], the humidity and temperature of airflow from exhalation and inhalation [5], chest and abdominal movement [6], transcutaneous CO_2 [7], oximetry probe (SpO_2) [8], *etc.* As opposed to contact monitoring methods, noncontact

monitoring methods do not reduce patient comfort. They mainly include radar-based respiration rate monitoring [9], optical-based respiration rate monitoring [10], and thermal sensor and imaging-based respiration rate monitoring [11]. However, their complex structure, reliance on external power sources, and discomfort restrict their application in health-monitoring devices.

In recent years, considerable attention has been devoted to developing comfortable wearable health monitoring electronic devices [12]. Piezoelectric and triboelectric materials have been successfully used in body-worn sensors and wearable electronics [13–17]. Piezoelectric nanogenerators (PENGs) and triboelectric nanogenerators (TENGs) can provide electrical power without the need for a battery because they can convert mechanical energy into electrical signals. In particular, TENG is a newly proposed energy harvester, which can generate electricity from mechanical energy produced by biomechanical motion or renewable green energy (e.g., wind, wave energy) based on the coupling effect, e.g. contact electrification and electrostatic induction [18–22]. Therefore, TENGs have great potential in self-powered wearable electronics [23–25]. For example, it has been used in healthcare monitoring systems for respiration behavior recognition, respiration rate monitoring, and respiratory disease detection [26]. Wang et al. [27] developed a self-powered real-time respiratory monitoring system with a TENG, but the TENG device only can distinguish different breathing patterns and record the respiration rate (*RR*). Zhao et al. [28] fabricated textile triboelectric nanogenerators (t-TENGs) as a wearable respiratory monitor by loom weaving metallic yarns into a weaving fabric. These devices can record *RR* and breathing depth. There are also other different TENG sensors for respiratory monitoring in health care [29–31] but most of them only demonstrate sensing ability and do not focus on sensing accuracy and practical feasibility with a miniatured dimension. Additionally, TENGs can be used to remove particulate matters (PMs) via electrostatic absorption created by the generated triboelectric charges, which is called triboelectric filtering [32]. TENGs integrated into an air filter have been used to provide electrostatic charge on the filter to attract small particles with higher efficiency [33–37].

In this paper, we present a changeable, self-powered, smart mask filter (respiratory monitoring) with nanofibers based on the principle of TENGs. The proposed respiration monitoring TENG (RM-TENG) combines monitoring respiration status and removing PMs. It consists of a polyacrylonitrile (PAN) and a polyvinylidene fluoride (PVDF) electrospun nanofiber mat. The reasons for choosing PAN and PVDF are: (i) they are suitable materials to make TENGs because of their different abilities to attain electrons [38,39]; (ii) nanofibers are also alternative materials as triboelectrification materials in wearable TENGs due to their flexibility and textured surface, which can increase the output voltage of the TENG [40–44]; (iii) compared with micro-fibrous filters, nanofibrous filters have higher filtration efficiency as they capture very small particulates due to the unique properties of nanofibers, such as small pore size, small diameter, and large specific surface area [45–47]. Compared to the applications that are introduced above, the developed RM-TENG can measure multiple respiratory timing indices other than *RR*, including inhalation time (t_{in}), exhalation time (t_{ex}), and their ratio ($IER = t_{in}/t_{ex}$), which requires great sensing accuracy. These respiratory timing indices can also provide more useful information about respiratory pathophysiology [48]. For example, they can be used to analyze the severity of chronic obstructive pulmonary disease (COPD) [49] and cystic fibrosis [49], and even to assess infant respiratory conditions [50].

Although contact area is an essential factor of the output performance of TENGs, it is challenging to calculate the effective contact area to analyze the output performance [51]. Therefore, in this paper, we employed 3D digital image correction (DIC) to characterize the deformation of nanofiber mats in the RM-TENG during the breathing process. Based on the deformation profile of the nanofiber mat, we created a mathematical model to calculate the contact area and described the relationships between the contact area and electrical output.

Furthermore, we also used a portable data acquisition device to capture and display the sensing signals with a miniaturized testing system, and a medical ventilator to examine the sensing accuracy of the RM-TENG. Lastly, the RM-TENG was attached to a commercial mask to monitor the respiratory conditions of the wearer while he was doing different physical exercises, which demonstrates its practical feasibility. Given the advantages of self-power, high filtration efficiency, and multi-indices monitoring, the nanofibrous mask filter based on TENGs shows excellent potential for cost-effective respiration monitoring. This paper also provides a new strategy for calculating the effective contact areas in TENGs.

2. Materials and methods

2.1. Materials

We prepared a PDVF electrospinning solution by dissolving 1.5 g PVDF powder (M_W = 534,000, Sigma-Aldrich) in a 10 ml solvent mixture of 40% N, N- dimethylformamide (DMF), and 60% acetone. A 12 wt% PAN solution was prepared by dissolving the PAN (M_w 90,000, Hangzhou Bay Acrylic Fiber Co., Ltd., China) powder in DMF. Both solutions were stirred with a magnetic stirrer at 50 °C for 10 h, which produced a homogeneous, transparent solution. DMF and acetone were purchased from Azur Chemicals (Hungary).

2.2. Electrospinning

The PVDF and PAN nanofibrous membranes were fabricated with a homemade single needle electrospinning setup. A syringe pump (Aitecs SEP-10S plus, Lithuania) supplied the polymer solution through a blunt-end stainless steel needle (inner diameter: 1.2 mm) from a 20 ml syringe at a certain feeding rate. The high voltage was provided by a DC high voltage generator (MA2000 NT 75/P, Hungary). Nanofibers were collected onto a rotating drum (diameter: 70 mm) covered by aluminum foil. The electrospinning process parameters for fabricating the PVDF membrane were: a feeding rate of 1.4 ml/h, a voltage of 25 kV, a collecting distance of 20 cm, and the drum rotation speed of 400 rpm. The electrospinning process parameters for fabricating the PAN membrane were: a feeding rate of 0.5 ml/h, a voltage of 25 kV, a collecting distance of 20 cm, and the drum rotation speed of 400 rpm. The relative humidity and ambient temperature during the experiments were 35 ± 2% and 25 ± 2 °C. The thickness of the nanofiber layer was controlled by the collecting time. We fabricated the PAN and the PVDF nanofibers with electrospinning collection time of 40 min, 80 min and 120 min; they are denoted as 40/80/120 min_PAN and 40/80/120 min_PVDF, respectively. The corresponding area density of the 40/80/120 min_PAN nanofiber layers are 0.38 g/m^2, 0.67 g/m^2 and 0.88 g/m^2; while 40/80/120 min_PVDF layers have the area density of 2.11 g/m^2, 3.04 g/m^2 and 3.88 g/m^2.

2.3. Characterization

The surface morphology of the nanofiber membrane was investigated with a scanning electron microscope (SEM) (JEOL 6380 LA, Japan). The surface was coated with a gold–palladium (Au-Pd) alloy for 30 s before it was examined by SEM. The diameter of the nanofibers was measured with the ImageJ program. It measured the diameter of 100 fibers in the SEM images. The texture of the nanofiber membranes was acquired with an atomic force microscope (AFM) (Flex AFM 5, Nanosurf, Switzerland). 3D digital image correlation (3D-DIC) (Monet 3D 2500, Sobriety, the Czech Republic) was used to detect the three-dimensional deformation of nanofiber membranes when they were blown. The DIC system consists of two 5 Mpixel cameras (MCR150-S, IDS GmbH., Obersulm, Germany) mounted on a tripod, two LED reflectors, and a computer with the Mercury RT software (Fig. S6). Before the test, the surface of the nanofiber membrane was sprayed with black speckles to
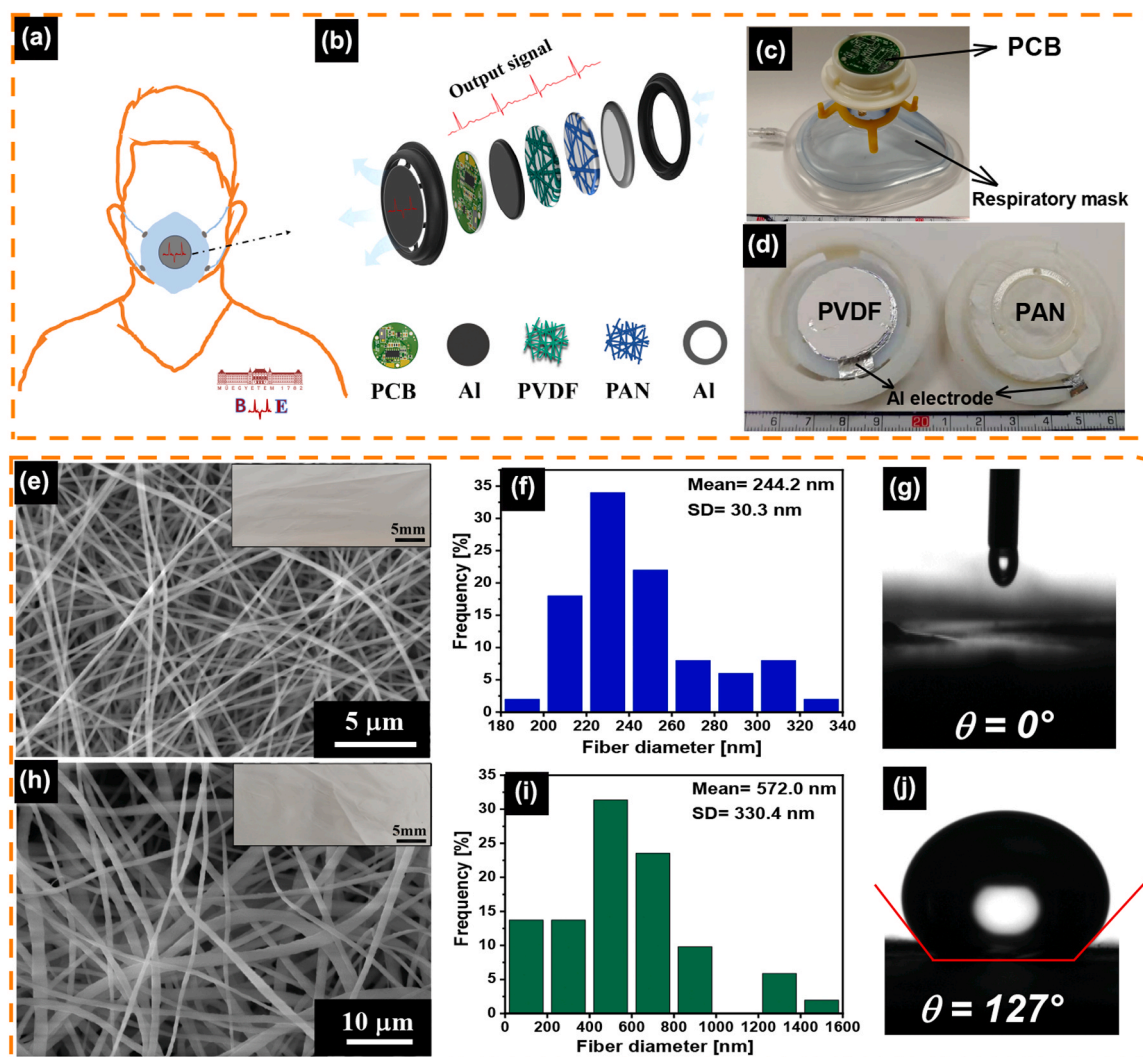
Fig. 1. (a-b) Schematic illustration of the RM-TENG; (c) Image of respiratory mask attached with RM-TENG; (d) The RM-TENG disassembled into two parts; (e) SEM image of PAN-NFM (inset is the photograph of the PAN-NFM); (f) The diameter distribution of PAN nanofibers; (g) Water contact angle on flat PAN-NFM; (h) SEM image of PVDF-NFM (inset is the photograph of the PVDF-NFM); (i) The diameter distribution of PVDF nanofibers; (j) Water contact angle on flat PVDF-NFM.

maximize contrast. The change in surface profile was measured with the stereo-vision system; it compared the 3D position of the black speckles on the undeformed membrane and the deformed membrane. The DIC tests were carried out at a flow velocity of 0.7 m/s within 60 s for all the circular samples with a diameter of 30 mm. The deformability of PAN and PVDF nanofiber layers with different thicknesses were tested with the same experimental parameters and conditions as stated above. Water contact angle measurements were performed with a drop shape analyzer (DSA30E, KRÜSS GmbH, Germany). In the measurements, the volume of the water droplet was approximately 10 μL. The electrical signals were acquired with a data acquisition device (34970 A, Keysight Technology, USA) and a portable data acquisition device (myDAQ, NI, USA). The myDAQ can be used as a digital multimeter, oscilloscope, and function generator controlled by LabView (NI, USA). LabView was used as the software platform for real-time data acquisition and analysis. The particle filtering properties of the nanoporous filters were analyzed with an aerosol particle counter (Lasair III 310 C, Artisan Technology Group, USA) (Fig. S12). It has six channels to detect the particle sizes of 0.3 μm, 0.5 μm, 1 μm, 5 μm, 10 μm, and 25 μm. The PM particles in the air of our laboratory had a broad size distribution ranging from < 300 nm to > 25 μm. The nanoporous filters were trimmed into a 35 mm diameter circle and fixed into the filter holder connected to the particle counter. All the tests were conducted with a constant airflow of 30 l/min, which is

approximately the average breathing flow of humans in a resting position. Pressure drop (*PD*) is one of the most important parameters indicating the performance of a filter. We built a simple measuring device to compare the breathability of nanofiber membranes with that of commercial masks, and the pressure drop of the membrane was measured at a predefined air mass flow rate, as shown in Fig. 5a. The trimmed circular membrane (diameter 30 mm) was fixed on the top of a tube with a cap. The bottom of the tube was connected to a water tap to supply water to the tube, which pushed the air inside to flow through the membrane fixed on the top at a certain flow velocity. A manometer (EMB-001, BME, Hungary) was used to measure the pressure difference (pressure drop) between pressure inside the tub and the atmospheric pressure (100,100 Pa). We used a medical ventilator (BEMHero2, BME, Hungary) developed by the university in our lab during the pandemic to examine the accuracy and consistency of the RM-TENG sensor by comparing the output results and the parameters provided by the ventilator. We carried out the on-body experiments with a treadmill (BH 5163270, Spain) to monitor the respiration parameters. The respiration parameters were recorded for 1 min immediately after the exercise. It can eliminate noise from wire vibrations during the exercise.

Informed Consent: The volunteer (Haijun He) agreed to take part in all the tests and be photographed for the manuscript with informed consent.
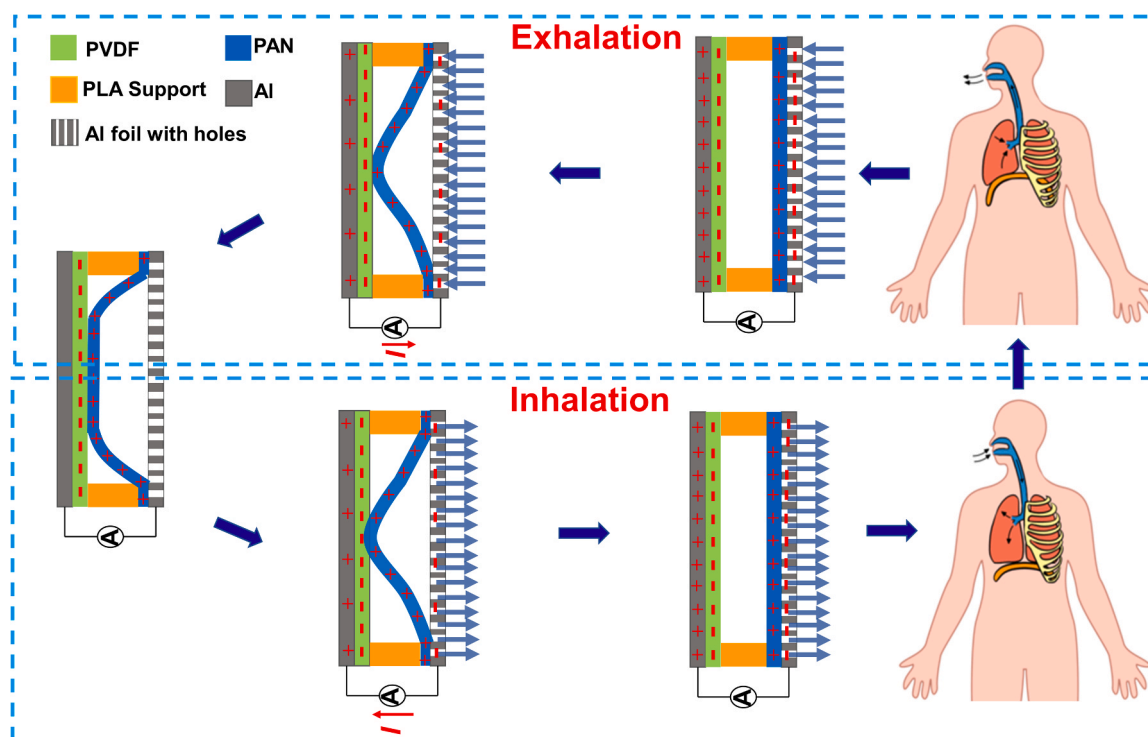
Fig. 2. Schematic illustration of the working mechanism of the breathing RM-TENG.

3. Results and discussion

3.1. Structural design of the RM-TENG

As schematically shown in Fig. 1a, the smart mask filter can be conveniently attached to a mask without contacting the wearer, and the wearer does not suffer from any discomfort. The mask filter has good breathability and filtration efficiency because it consists of two nanofibrous layers. Fig. 1b illustrates the detailed structure of the RM-TENG. It includes two nanofiber mats, and the conductive aluminum films as the electrodes; in addition, a miniature printed circuit board (PCB) was designed to collect and transmit the data. The entire monitoring system with the RM-TENG integrated into a respiratory mask is illustrated in Fig. 1c. Fig. 1d shows photograph of the disassembled RM-TENG. The Al foil and the PAN nanofiber layer is fixed together with a washer to have a close contact (Fig. S1). The PAN and PVDF nanofiber membranes (NFM) were fabricated via electrospinning, as illustrated in Fig. S2.

The morphology of the PAN and PVDF nanofibers was observed by SEM, as shown in Fig. 1e and h. The insets are the photos of the produced nanofiber mat from PAN and PVDF, respectively. Fig. 1f and i show that PAN nanofibers have a smaller diameter (244.2 nm) than PVDF nanofibers (572.0 nm). We also examined their wettability by placing a water droplet onto them. The water contact angle on the PAN and PVDF NFM are 0° and 127°, respectively (Fig. 1g and j). They have a nanosized surface structure, which is suitable for charge generation in TENGs. Besides, their good flexibility and robust mechanical properties render them as suitable materials for breathing sensors because they can be easily actuated by breathing. In addition, nanofiber mats possess good breathability and filtration efficiency (the most important properties of a mask filter) because of their nanosized porous structure. Therefore, we chose electrospun nanofiber mats as filter materials and also as dielectric materials for sensing purposes.

3.2. Working mechanism of the RM-TENG

The working principle and sensing mechanism of the RM-TENG are illustrated in Fig. 2. The two nanofiber mats are actuated by the air flow of breathing periodically and contact and separate from each other, which converts the breathing motion into electric signals by the RM-TENG. The recorded signals are processed to characterize the respiration state. The breathing–electric conversion is mainly based on the coupling effect of contact electrification and electrostatic induction. In the original state, there are no charges transported between the two friction layers. During exhalation, the PAN-NFM is blown and gets into contact with the PVDF-NFM. Due to the different electron affinities of PAN and PVDF, the PAN nanofiber layer loses electrons and becomes positive in the contact process, while the PVDF layer gains electrons to generate negative charges. When the exhalation process is finished, the TENG reaches an equilibrium state, where all the induced charges are neutralized, and there is electric potential difference between the electrodes because all the charges stay at the contact surfaces. When inhalation starts, the PAN layer is sucked toward its original position, and the two layers begin to separate from each other. An electric potential difference between the two electrodes is generated, and the electrons flow back from the PVDF layer to the PAN layer, generating current in the opposite direction. When the PAN-NFM returns to its original state and separates from PVDF-NFM, the electrons stop flowing and the TENG reaches an electrostatic equilibrium. Therefore, an alternating current can be generated during a breathing cycle. Meanwhile, the PAN-NFM also serves as a filter to capture the small aerosol particles from the air.

3.3. Electrical output performance of the RM-TENG

To use the smart filter for respiration monitoring, we systematically studied the output performance of RM-TENGs with different structural parameters. To evaluate the output performance, we used a shaker with a constant frequency (250 rpm) to mimic the "inhalation-exhalation" process. The shaker periodically squeezed a wash bottle connected to the RM-TENG, as shown in Fig. S3. Fig. 3a shows the corresponding voltage when different materials are used as the tribo-positive counterpart, such as aluminum (Al), polyethylene terephthalate (PET), and PAN. In comparison, the voltage output of the RM-TENG had a maximum value of
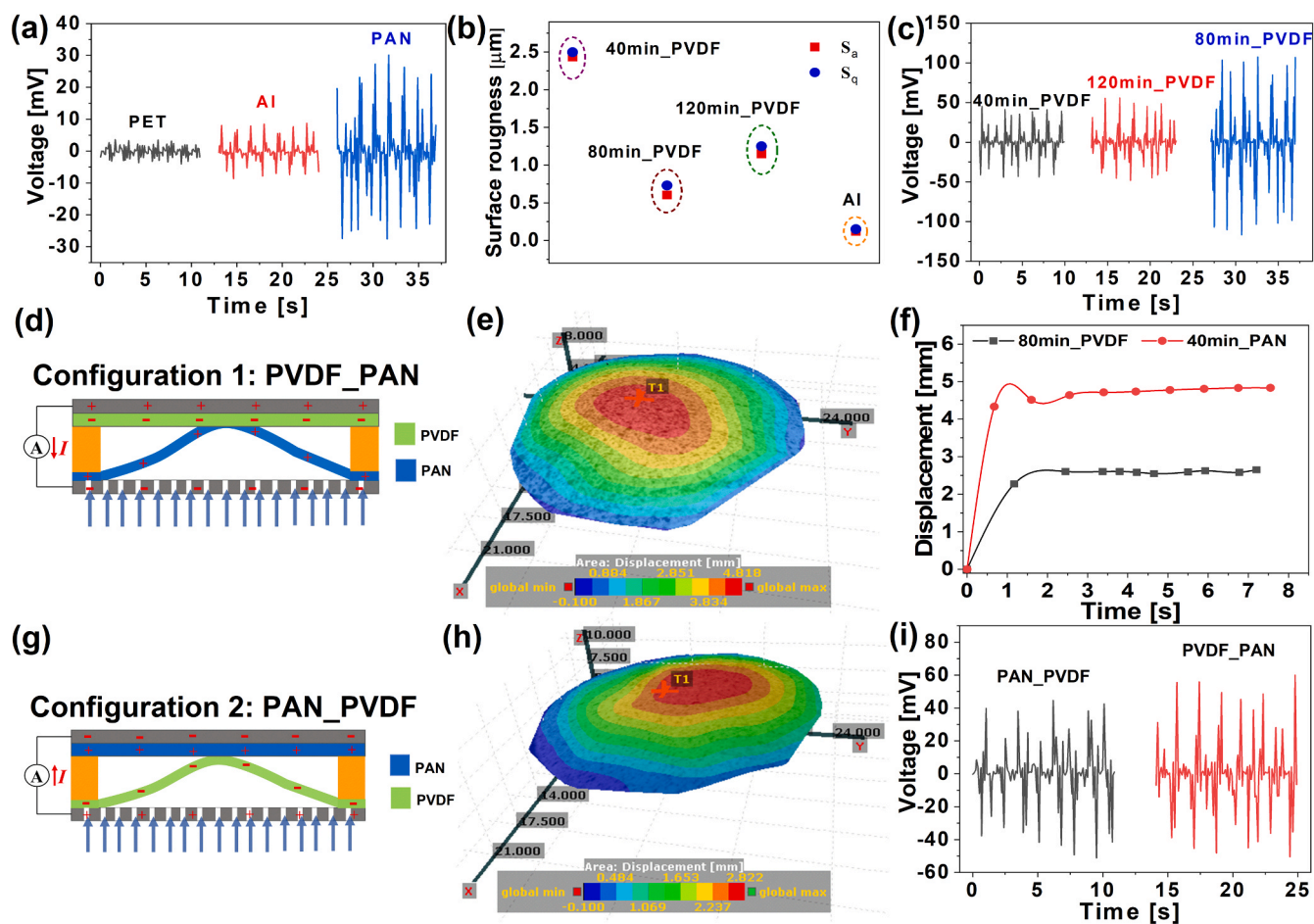
Fig. 3. (a) Voltage output of the RM-TENG with different contact materials; (b) The roughness parameters (R_a, R_q) of the PVDF-NFM with different thicknesses and the Al foil; (c) The voltage output of the RM-TENG with various PVDF nanofiber thicknesses; (d) (e) 3D deformation profile of 40min_PAN-NFM recorded by DIC. (f) The displacement of the center point of the nanofiber membranes; (g) Configuration 2: the PVDF nanofiber layer is the deformed layer; (h) 3D deformation profile of 80min_PVDF-NFM recorded by DIC; (i) The voltage output of the TENG with two configurations.

~30 mV when a PAN-NFM was used as the friction counterpart. Therefore, the PAN-NFM was selected as the friction counterpart in the RM-TENG in the following experiments.

The influence of the texture of the nanofiber layer on the voltage was explored through voltage signal testing. The surface texture of the PVDF-NFM and the Al foil were characterized by AFM, showing that the PVDF-NFM with different thicknesses had obvious differences in surface topology, as shown in Fig. S4 and S5. With the comparison of the surface morphology of the PVDF-NFM and the Al foil, we found that the PVDF-NFM can be considered planar isotropic by means of roughness, while the Al foil has different roughness in the manufacturing direction (R_a(M)= 0.08 μm) and the perpendicular direction (R_a(P)= 0.15 μm). Fig. 3b displays the root average arithmetic roughness (R_a), and root mean surface roughness (R_q) of the PVDF-NFMs with different thicknesses. We found that R_a and R_q of the 80 min PVDF-NFM were 0.60 μm and 0.73 μm, respectively, and the 40 min PVDF-NFM had the maximum roughness. It is because the collected nanofiber layer on the collector has a compactness gradient along its thickness with the increase of electrospinning time. At the beginning of electrospinning, the nanofibers can be tightly attracted to the collector, but the nanofibers are not enough to fully cover the flat collector surface, resulting in significant height differences at different locations. With time going, more and more nanofibers are collected on the flat surface to achieve a uniform distribution with a smaller roughness. But when the electrospinning time is further increased, the electrical forces can be reduced due to the isolation provided by the more and more nanofibers on the collector,

resulting in a fluffy structure on the top of the nanofiber layer. In this case, the fluffy structure at the surface can result in higher roughness and deteriorate the voltage output.

Fig. 3c shows the variations of the voltage output of the RM-TENG with the different textures of the PVDF nanofiber layer. As can be seen, the voltage generated by the RM-TENG increases as surface roughness decreases; it is easier to have a large and flat contact area when the surface of the PVDF nanofiber layer is smoother, which is also consistent with results published in the literature [52].

During the same "inhalation-exhalation" mimicking process, we measured a series of voltage outputs generated with two different configurations of the PVDF and PAN nanofiber layers. Due to the different deformability of nanofiber mats, it is essential to optimize the voltage output of the RM-TENG with a different nanofiber mat as the deformed layer. Fig. 3d and g show the two configurations of PAN and PVDF nanofiber layers. We also recorded the deformation processes of the nanofiber layers using 3D DIC (Fig. S6 and **Video S1**). As shown in Fig. 3e, f and h, the center of the PAN-NFM has greater displacement than that of the PVDF-NFM during the deformation process. Fig. 3i shows that when the PAN-NFM was used as the deformed layer, the RM-TENG produced a voltage output of ~110 mV, which was slightly higher than when the PVDF-NFM was used at a constant gap distance of 2 mm. It can be attributed to the larger contact areas between the two nanofiber layers, which is consistent with the displacement results in Fig. 3f.

Supplementary material related to this article can be found online at. We also investigated the effects of the gap distance between the two
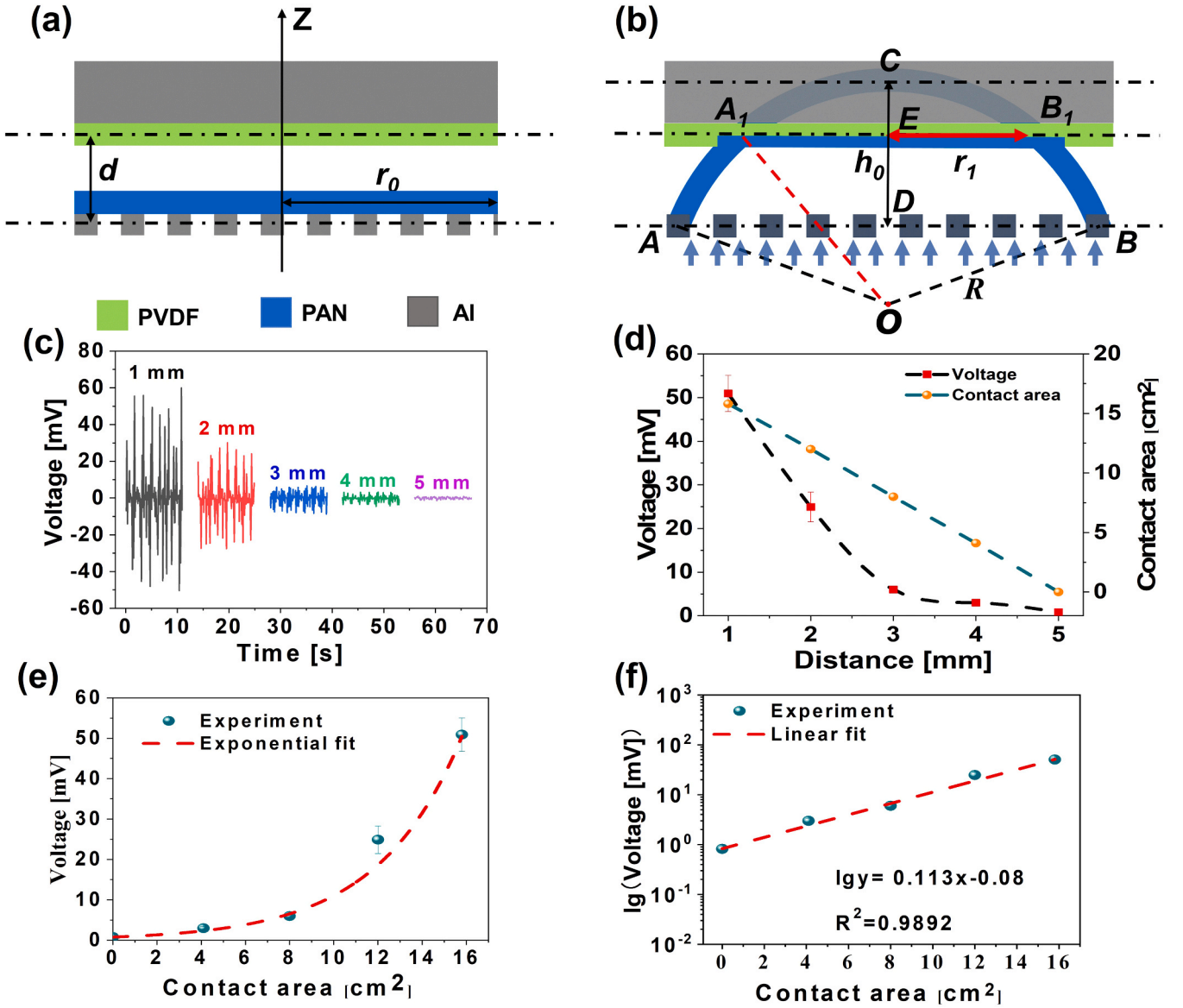
Fig. 4. Schematics of (a) Separation and (b) Contact state of the RM-TENG; (c) The voltage output of the RM-TENG with various gap distances; (d) The effects of gap distance on the voltage output and the contact area; (e) Voltage output as a function of contact area. (f) lg Voltage output as a function of contact area. The red dashed lines represent the fitting curves.

surfaces on the generated voltage. In the experiments, we chose configuration 1 (PVDF_PAN), the gap distance between the two layers was adjusted from 0 to 5 mm by the spacers, because the maximum displacement of the PAN nanofiber layer is around 5 mm according to the DIC results. Fig. 4a and b show the 2D schematics of the contact and separation state of the RM-TENG with the deformation profile of the 40 min_PAN nanofiber layer. In the drawings, d denotes the gap distance between the surfaces of the electrode layer and the nanofiber layer, r_1 is the radius of the nanofiber sample (25 mm), h_0 is the maximum displacement of the nanofiber layer (5 mm). r_0 represents the radius of the contact region between the two surfaces. When gap distance d is larger than the maximum displacement $h_0(d \geq 5mm)$, r_0 is zero. When the gap distance is zero, $r_0 = r_1 = 25mm$. Since the electrode layer and nanofiber layer are quite thin compared with the gap distance, their thicknesses are neglected in the calculations. Fig. 4a shows the original state of the nanofiber layer before being blown. In Fig. 4b, the 2D deformed profile of the nanofiber layer is regarded as an arched shape. The arc $\overset{\frown}{ACB}$ is considered as the deformed shape of the nanofiber layer; C is the center point with maximum displacement after the deformation.

Therefore, the arc radius can be calculated by Eq. (1):

$$R = |\overrightarrow{OB}| = (r_0^2 + h_0^2)\big/2h_0 \tag{1}$$

The vector $\overrightarrow{A_1B_1}$ denotes the position of the upper nanofiber layer. The same arc radius can also be calculated by Eq. (2).

$$R = |\overrightarrow{OA_1}| = (r_1^2 + (h_0 - d)^2)\big/2(h_0 - d) \tag{2}$$

Where r_1 is the radius of the contacting area of the two nanofiber membranes, which can be derived based on Eqs. (1) and (2), and expressed as Eq. (3):

$$r_1 = \sqrt{\frac{h_0 - d}{h_0}(r_0^2 + h_0^2) - (h_0 - d)^2} \tag{3}$$

The effective contacting area S can be determined by the gap distance between the two surfaces, as shown in Eq. (4):
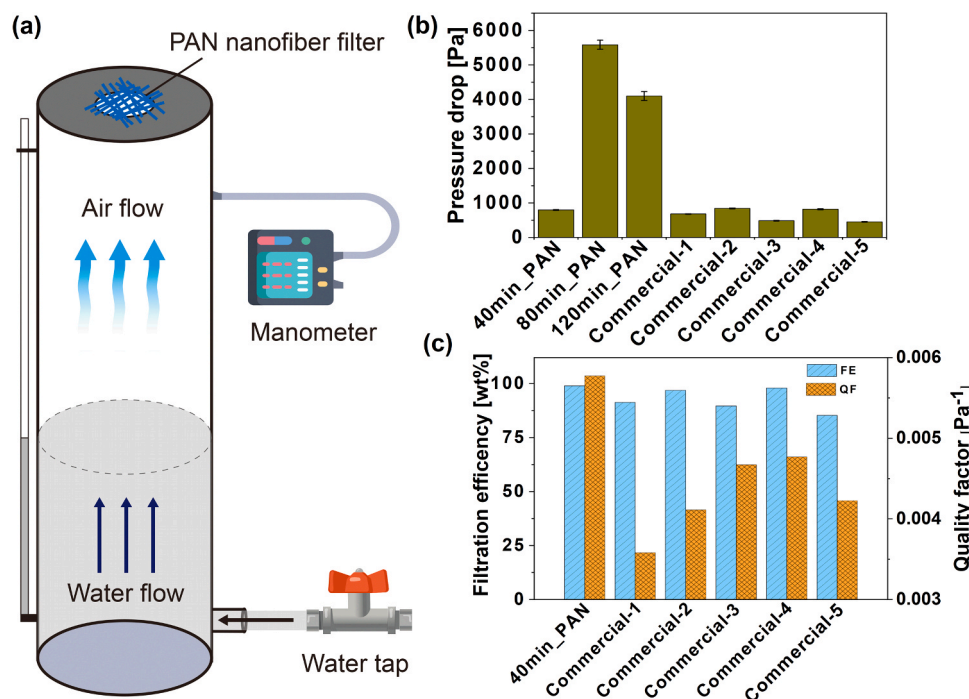
Fig. 5. (a) Schematic illustration of our homemade pressure drop testing setup. (b) The pressure drops of the PAN-NFMs and commercial masks. (c) Filtration efficiency and quality factor of the PAN-NFMs and commercial face masks.

$$S = \pi r_1^2 = \pi \left[\frac{h_0 - d}{h_0} \left(r_0^2 + h_0^2 \right) - (h_0 - d)^2 \right] \qquad (4)$$

Eq. (4), shows that the contacting area *S* depends on the gap distance between the two surfaces, showing negative correlation with the gap distance.

Fig. 4c shows the voltage output of the RM-TENG with different gap. The voltage tends to decrease with the increase of the gap distance. This is mainly because when the gap distance is larger, the contact region between the two nanofiber layers is smaller (as shown in Fig. 4d), thus the contact area is sensitive to the gap distance. Fig. 4e and f illustrate the voltage change curve of the RM-TENG with different contact areas. It shows that the RM-TENG is more sensitive to change in the contact area when the area is bigger. It is probably caused by the high specific area of the nanofibers because the effective contact area includes the superficial area of the contact area and the specific area of the nanofibers. When the contact area is larger, there are more nanofibers with high surface area there to contribute to the effective contact area.

3.4. Filtration efficiency and breathability analysis

To compare the breathability of nanofiber membranes with that of commercial masks, we measured their pressure drop at a predefined air mass flow rate (see Fig. 5a). Fig. 5b shows the *PD* results measured with an airflow velocity of 0.7 m/s. The *PD* increases with increasing nanofiber membrane thickness, suggesting that air permeability decreases. Besides, five commercial respirator masks (KN95, N95, and FFP2 masks) were tested for comparison. PAN-NFM (40 min) shows less *PD* (797.5 Pa) than commercial-2 (843.9 Pa) and commercial-4 (819.2 Pa). However, the PAN-NFMs (80 min and 120 min) have the worst breathability with a *PD* of more than 4000 Pa, so they are not suitable as a mask filter. It is because the nanofiber membrane has greater area density and less porosity with a longer electrospinning time. Then, we measured the filtration efficiency (*FE*) of PAN-NFMs and five commercial masks with the same flow velocity as used in the pressure drop tests. The detailed definition of filtration efficiency (FE) is presented in **Note S1**. Fig. 5c shows the *FE* of the PAN-NFM (40 min) reaches 99.00 wt%,

which is better than the *FE* of the five commercial masks (Table S1). Fig. S7 shows that the nanofiber membrane still has the highest filtration efficiency (99.64 n%) for particle sizes between 0.3 and 0.5 µm (Table S2). However, we could not successfully measure the *FE* of the PAN-NFMs (80 min and 120 min) because they were too dense to allow airflow at the required flow rate during the filtration test. They also had the worst breathability. To quantitatively analyze the overall filtration performance of the filter considering both *FE* and *PD*, we used the quality factor (*QF*). It can be calculated with the equation below [53, 54]:

$$QF = -\ln(1 - \eta)/\Delta P, \qquad (5)$$

where *η* represents filtration efficiency (wt%), and *ΔP* represents the *PD*. Usually, a higher *QF* value indicates better filtration performance of the filter[37]. The *QF* values of the nanofiber membrane and the commercial masks are shown in Fig. 4c (also in Table S1). The PAN-NFM (40 min) has a higher *QF* than the five commercial masks, even twice the *QF* of the commercial-1 mask. The PAN-NFM (40 min) is suitable for mask filter application; its filtration behavior is comparable to that of the commercial face masks.

3.5. Application of the RM-TENG for respiration monitoring

To demonstrate the capability and accuracy of the RM-TENG sensor for monitoring the respiratory state of a subject, we connected it to a medical ventilator which our faculty developed during the COVID-19 pandemic, as shown in Fig. 6a-1. More importantly, a small-sized data acquisition device was used in the following studies, which can provide the potential to miniaturize the sensing system to fit into a mask vent. We 3D printed two funnel-shaped structures from PLA for the ventilator to provide the breathing cycles for the RM-TENG (Figs. 6a-2). The large end was covered with a nanofiber mat and a hollow Al film as the electrode, and they were assembled by screws. They were separated by a PLA spacer with adjustable thickness, as shown in Figs. 6a–3. Then, one of the smaller ends was connected to the air inlet of the ventilator for "exhalation", and another end was connected to a balloon. During the
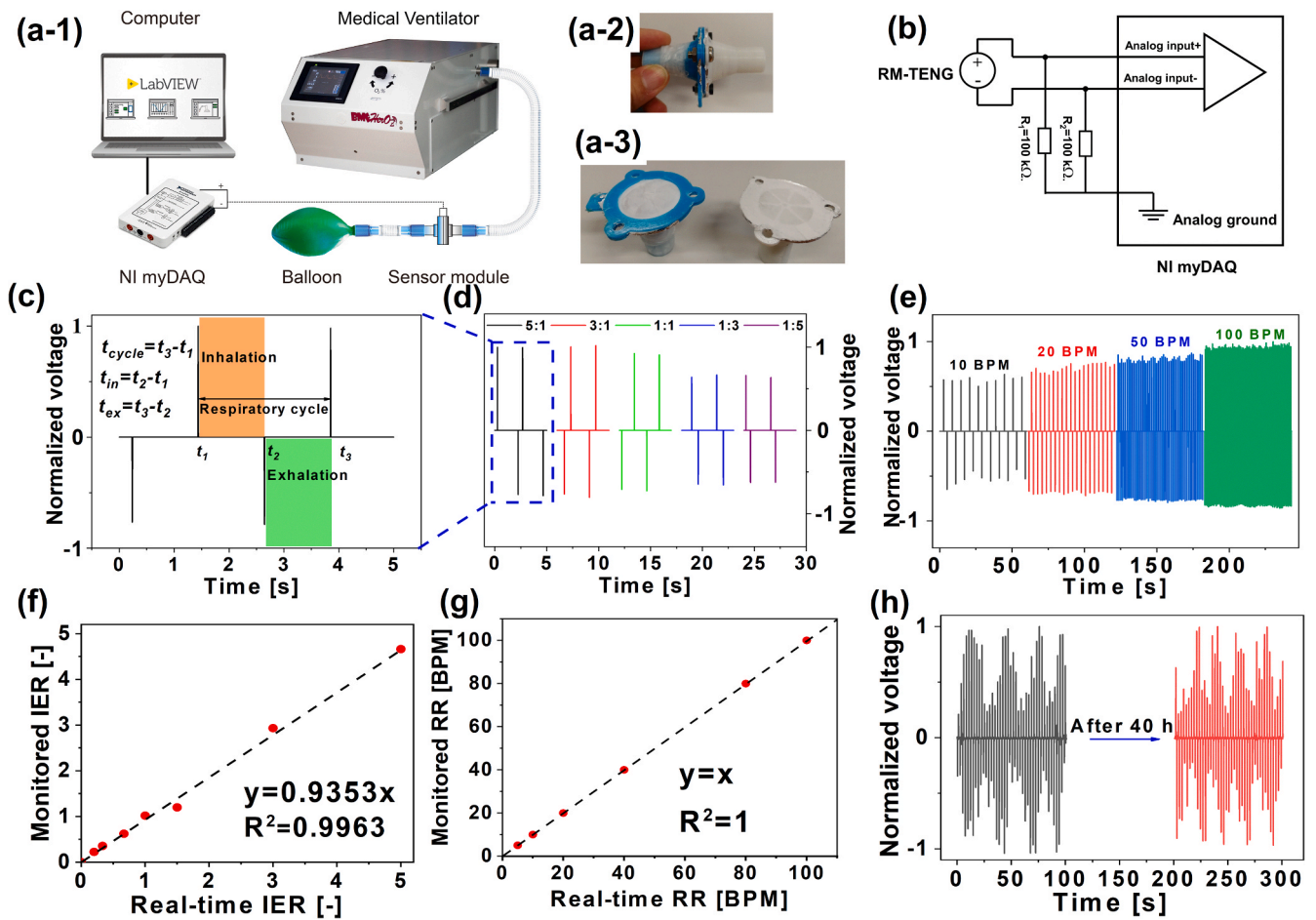
Fig. 6. (a-1) Illustration of the respiration testing system with a ventilator. (a-2) The assembled sensor. (a-3) The two components of the sensor used on the ventilator. (b) Working principle of the signal testing system with NI myDAQ; (c) The magnified breathing cycle recorded by the RM-TENG. (d) Normalized voltage corresponding to various *IERs*; (e) Comparison of real-time *IER* set at the medical ventilator and the *IER* monitored by the RM-TENG, with the use of regression analysis; (f) Normalized voltage corresponding to different *RRs*; (g) Comparison of real-time *RR* set at the medical ventilator and the *RR* monitored by the RM-TENG with the use of regression analysis; (h) Long-term performance of the RM-TENG connected to the medical ventilator.

"exhalation" process, the air from the ventilator inflated the balloon; when the "exhalation" stopped, the inflated balloon started to recover its original shape and squeezed the air back to the ventilator, which was considered the "inhalation" process. To miniaturize the testing system, we used a portable data acquisition device (myDAQ) that uses the NI LabVIEW-based software to measure and analyze the voltage signals. In the testing process, two 100 kΩ resistors connected the negative input and positive input to the analog ground to balance noise signals from the differential signal source, as shown in Fig. 6b.

The medical ventilator can adjust the most important respiratory parameters, which are respiratory rate (*RR*), inhalation time (t_{in}), exhalation time (t_{ex}), and their ratio (*IER*). Sensing accuracy can be assessed by comparing the recorded respiratory results from the sensor with the input respiratory parameters of the ventilator. One of the respiratory cycles is magnified in Fig. 6c. As shown in Fig. S8, one complete typical breathing cycle includes a positive voltage peak and a negative voltage peak with the peak width around 10 ms, generated by inhalation and exhalation, respectively. The peak-to-peak interval between the two adjacent positive (or negative) peaks is the breathing cycle time (t_{cycle}). Thus, *RR* can be defined by:

$$RR = 60/t_{cycle} \text{ (breaths per minute) (BPM)} \quad (6)$$

The time delays between the negative peak and its two adjacent positive peaks are defined as t_{in} and t_{ex} respectively, which can be used to calculate the *IER* as the following:

$$IER = t_{in}/t_{ex} \quad (7)$$

As shown in Fig. 6c-e, all the positive and negative voltage peaks of respiration are recorded. All the captured signals are clear enough to be identified in all the breathing processes with various respiratory states. To measure the accuracy of our RM-TENG, we compared the monitored *RR* and *IER* with the real-time input parameters of the ventilator. Fig. 6f shows the correlation plot of monitored *IER* and real-time *IER*. The RM-TENG shows a R^2 of 0.9963 with the real-time parameter, which indicates the monitored results have a significant linear correlation with real-time *IER*. The slope of the linear fitting is 0.9353, which indicates that all the monitored *IER* values have a 93.53% agreement with the real-time *IER* values. Moreover, the linear fitting in Fig. 6g shows a correlation coefficient of $R^2 = 1$ and a fitting slope of 1, which demonstrates the monitored *RR* values are the same as real-time *RR* values. This indicates that our RM-TENG measures *RR* and *IER* with excellent stability and accuracy (see Fig. S9, S10, and **Video S2**). Stability and durability are of great importance for practical applications; therefore, we tested the durability of the RM-TENG by comparing its performance with its initial performance after 40 h. Fig. 6 h shows that no missing peaks can be observed after 40 h, indicating adequate stability and durability. To verify the respiration monitoring capability of the RM-TENG sensor, we further developed an entire respiratory monitoring system, including a RM-TENG sensor, a microcontroller unit, a charge amplifier, a display screen, or a cellphone with Bluetooth (Fig. S11 and
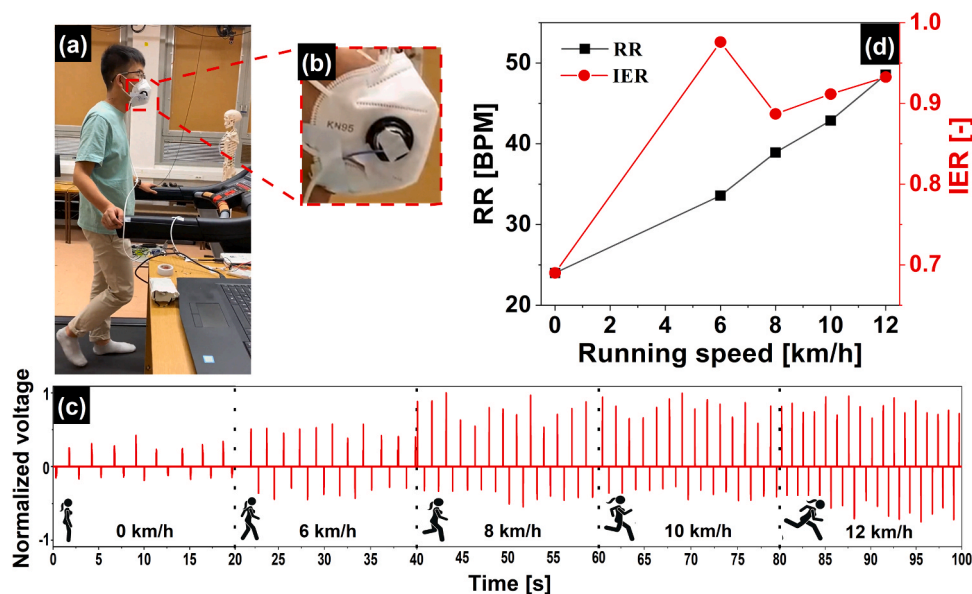
Fig. 7. (a) Photo of the subject walking on the treadmill with a mask attached to the RM-TENG. (b) The enlarged mask attached to the RM-TENG. (c) The signal waveforms recorded by the RM-TENG after the subject walked/ran on the treadmill at various speeds. (d) The real-time *RR* and *IER* obtained from the RM-TENG after the subject walked/ran on the treadmill at various speeds (only 20 s of data recording at each test is displayed for the clear peaks and frequencies).

Video S3). In the system, the RM-TENG sensor can record the real-time respiratory signals based on the changes of respiratory state without any additional power source. It demonstrates that the entire monitoring system can be integrated into a miniaturized module and attached to a commercial mask as a self-powered real-time respiratory monitoring device.

Supplementary material related to this article can be found online at.

Furthermore, to study the practical application of the RM-TENG sensor for respiration monitoring, we attached our RM-TENG to a commercial mask, as shown in Fig. 7a. Fig. 7b shows that it is straightforward and convenient to attach and change the filter without direct contact with the wearer. We used a treadmill to precisely adjust the pace to conduct on-body experiments (**Video S4**). To avoid the noise from the vibration of the wires during the exercise, we started recording the signal immediately after a 5-min exercise, but breathing was the same as during the exercise. Fig. 7c shows the detected breathing signals after treadmill exercise of various speeds (i.e., from walking to fast running). Based on the recorded voltage curves at different speeds, we calculated the average values of *RR* and *IER* afterward, based on the recorded signals. They demonstrated that the *RR* of the subject increased when his walking/running speed increased. And the *IER* increases and reaches around 1.0 after the exercise. At the same time, the *RR* was 24 BPM, and *IER* was 0.69 when the subject was at rest, which is within the range of an average person. The measured results clearly present that the RM-TENG is able to monitor the wearer's respiratory states with multiple respiratory indices. For the stable application during exercise, it would need further technology development, which is a future task and goal.

Supplementary material related to this article can be found online at.

4. Conclusion

In summary, we designed a self-powered, changeable mask filter with high filtration efficiency based on a triboelectric nanogenerator for respiration monitoring. We systematically characterized the impacts of structure parameters (i.e. material types, gap distance, membrane thickness, and configuration of the membranes) on the voltage output of the RM-TENG. We analyzed the effects of gap distance between the two nanofiber layers on the effective contact area and the voltage output, and constructed a mathematical model to reveal the correlation between the gap distance and the contact area. The optimized structure parameters for our RM-TENG are the following: PAN nanofiber mat used as positive triboelectric layer, a gap distance of 1 mm, a PVDF nanofiber mat with 80 min collection time, and a 4PAN nanofiber mat with 40 min collection time used as the deformed layer. The fabricated RM-TENG exhibits good sensing accuracy and durability in monitoring respiration, which was proved with a medical ventilator with known input respiration parameters. In addition, the RM-TENG built with the optimized structure parameters exhibited high filtration efficiency (99 wt %), which is better than that of some commercial masks. We conducted on-body tests to continuously monitor the respiration signals after various exercise intensities. The detected signals demonstrated that the *RR* and *IER* increased with increasing walking/running speed of the subject. The *RR* and *IER* of the subject at rest was measured by the RM-TENG; they were 24 BPM and 0.69, respectively. Our results indicate that the smart mask filter based on a triboelectric nanogenerator has significant potential in respiration monitoring for health care.

CRediT authorship contribution statement

Haijun He: Conceptualization, Investigation, Methodology, Software, Validation, Visualization, Funding acquisition, Writing - original draft. **Jian Guo:** Investigation, Methodology, Software. **Balázs Illés:** Investigation, Software. **Attila Géczy:** Investigation, Software. **Balázs Istók:** Investigation. **Viktor Hliva:** Investigation. **Dániel Török:** Investigation. **József Gábor Kovács:** Project administration, Funding acquisition. **István Harmati:** Investigation. **Kolos Molnár:** Supervision, Funding acquisition, Resources, Writing - review & editing.

Declaration of Competing Interest

The authors declare that they have no known competing financial interests or personal relationships that could have appeared to influence the work reported in this paper.

Acknowledgments

Appendix A. Supporting information

Supplementary data associated with this article can be found in the online version at doi:10.1016/j.nanoen.2021.106418.

References

[1] T. Czigány, F. Ronkay, The coronavirus and plastics, Express Polym. Lett. 14 (6) (2020) 510–511, https://doi.org/10.3144/expresspolymlett.2020.41.

[2] F.Q. Al-Khalidi, R. Saatchi, D. Burke, H. Elphick, S. Tan, Respiration rate monitoring methods: a review, Pediatr. Pulmonol. 46 (6) (2011) 523–529, https://doi.org/10.1002/ppul.21416.

[3] G.M. Yuill, D. Saroya, S.L. Yuill, A national survey of the provision for patients with latex allergy, Anaesthesia 58 (2003) 775–803, https://doi.org/10.1046/j.1365-2044.2003.03256.x.

[4] A. Yadollahi, Z. Moussavi, Acoustic obstructive sleep apnea detection, 31st Annual International Conference of the IEEE EMBSMinneapolis, Minnesota, USA, 2009 4. https://doi.org/10.1109/IEMBS.2009.5332870.

[5] M. Folke, L. Cernerud, M. Ekstrom, B. Hok, Critical review of non-invasive respiratory monitoring in medical care, Med. Biol. Eng. Comput. 41 (2003) 377–383, https://doi.org/10.1007/BF02348078.

[6] K. Nepal, E. Biegeleisen, T. Ning, Apnea detection and respiration rate estimation through parametric modelling, IEEE 28th Annu. Northeast Bioeng. Conf. USA (2002) 277–278, https://doi.org/10.1109/NEBC.2002.999573.

[7] T. Lee-Chiong. Sleep: A Comprehensive Handbook, First ed., John Wiley and Sons Inc, Hoboken, New Jersey, 2006.

[8] D. Wertheim, C. Olden, E. Savage, P. Seddon, Extracting respiratory data from pulse oximeter plethysmogram traces in newborn infants, Arch. Dis. Child. Fetal Neonatal Ed. 94 (4) (2009) F301–F303, https://doi.org/10.1136/adc.2008.145342.

[9] E.F. Greneker, Radar sensing of heartbeat and respiration at a distance with applications of the technology, Radar 97 (1997) 150–153, https://doi.org/10.1049/cp:19971650.

[10] H. Aoki, Y. Takemura, K. Mimura, M. Nakajima, Development of non-restrictive sensing system for sleeping person using fiber grating vision sensor, MHS2001. Proceedings of 2001 International Symposium on Micromechatronics and Human ScienceNagoya, Japan, 2001. https://doi.org/10.1109/MHS.2001.965238.

[11] C. Hsu, J.C. Chow, Design and clinic monitoring of a newly developed non-attached infant apnea monitor, Biomed. Eng., Basis Commun. 17 (2005) 16–24, https://doi.org/10.4015/16237205000202.

[12] T.Q. Trung, N.E. Lee, Flexible and stretchable physical sensor integrated platforms for wearable human-activity monitoringand personal healthcare, Adv. Mater. 28 (22) (2016) 4338–4372, https://doi.org/10.1002/adma.201504244.

[13] Z. Li, M. Zhu, J. Shen, Q. Qiu, J. Yu, B. Ding, All-fiber structured electronic skin with high elasticity and breathability, Adv. Funct. Mater. 30 (6) (2019), 1908411, https://doi.org/10.1002/adfm.201908411.

[14] X. Wang, W.Z. Song, M.H. You, J. Zhang, M. Yu, Z. Fan, S. Ramakrishna, Y.Z. Long, Bionic single-electrode electronic skin unit based on piezoelectric nanogenerator, ACS Nano 12 (8) (2018) 8588–8596, https://doi.org/10.1021/acsnano.8b04244.

[15] X. Peng, K. Dong, C. Ye, Y. Jiang, S. Zhai, R. Cheng, D. Liu, X. Gao, J. Wang, Z.L. Wang, A breathable, biodegradable, antibacterial, and self-powered electronic skin based on all-nanofiber triboelectric nanogenerators, Sci. Adv. 6 (2020) eaba9624, https://doi.org/10.1126/sciadv.aba9624.

[16] Y. Xin, J. Zhu, H. Sun, Y. Xu, T. Liu, C. Qian, A brief review on piezoelectric PVDF nanofibers prepared by electrospinning, Ferroelectrics 526 (1) (2018) 140–151, https://doi.org/10.1080/00150193.2018.1456304.

[17] S. Chen, J. Jiang, F. Xu, S. Gong, Crepe cellulose paper and nitrocellulose membrane-based triboelectric nanogenerators for energy harvesting and self-powered human-machine interaction, Nano Energy 61 (2019) 69–77, https://doi.org/10.1016/j.nanoen.2019.04.043.

[18] K. Dong, J. Deng, Y. Zi, Y.C. Wang, C. Xu, H. Zou, W. Ding, Y. Dai, B. Gu, B. Sun, Z.L. Wang, 3D orthogonal woven triboelectric nanogenerator for effective biomechanical energy harvesting and as self-powered active motion sensors, Adv. Mater. 29 (38) (2017), https://doi.org/10.1002/adma.201702648.

[19] Z.L. Wang, A.C. Wang, On the origin of contact-electrification, Mater. Today 30 (2019) 34–51, https://doi.org/10.1016/j.mattod.2019.05.016.

[20] J. Wang, C. Wu, Y. Dai, Z. Zhao, A. Wang, T. Zhang, Z.L. Wang, Achieving ultrahigh triboelectric charge density for efficient energy harvesting, Nat. Commun. 8 (1) (2017) 88, https://doi.org/10.1038/s41467-017-00131-4.

[21] H. Xue, Q. Yang, D. Wang, W. Luo, W. Wang, M. Lin, D. Liang, Q. Luo, A wearable pyroelectric nanogenerator and self-powered breathing sensor, Nano Energy 38 (2017) 147–154, https://doi.org/10.1016/j.nanoen.2017.05.056.

[22] K. Xia, J. Fu, Z. Xu, Multiple-frequency high-output triboelectric nanogenerator based on a water balloon for all-weather water wave energy harvesting, Adv. Energy Mater. 10 (2020), 2000426, https://doi.org/10.1002/aenm.202000426.

[23] K. Xia, Z. Zhu, H. Zhang, C. Du, Z. Xu, R. Wang, Painting a high-output triboelectric nanogenerator on paper for harvesting energy from human body motion, Nano Energy 50 (2018) 571–580, https://doi.org/10.1016/j.nanoen.2018.06.019.

[24] K. Xia, D. Wu, J. Fu, Z. Xu, A pulse controllable voltage source based on triboelectric nanogenerator, Nano Energy 77 (2020), 105112, https://doi.org/10.1016/j.nanoen.2020.105112.

[25] K. Xia, D. Wu, J. Fu, N.A. Hoque, Y. Ye, Z. Xu, A high-output triboelectric nanogenerator based on nickel–copper bimetallic hydroxide nanowrinkles for self-powered wearable electronics, J. Mater. Chem. A 8 (48) (2020) 25995–26003, https://doi.org/10.1039/d0ta09440d.

[26] J. Li, Y. Long, F. Yang, X. Wang, Respiration-driventriboelectric nanogenerators for biomedical applications, EcoMat 2 (3) (2020), https://doi.org/10.1002/eom2.12045.

[27] M. Wang, J. Zhang, Y. Tang, J. Li, B. Zhang, E. Liang, Y. Mao, X. Wang, Air-flow-driven triboelectric nanogenerators for self-powered real-time respiratory monitoring, ACS Nano 12 (6) (2018) 6156–6162, https://doi.org/10.1021/acsnano.8b02562.

[28] Z. Zhao, C. Yan, Z. Liu, X. Fu, L.M. Peng, Y. Hu, Z. Zheng, Machine-washable textile triboelectric nanogenerators for effective human respiratory monitoring through loom weaving of metallic yarns, Adv. Mater. 28 (46) (2016) 10267–10274, https://doi.org/10.1002/adma.201603679.

[29] Z. Liu, Z. Zhao, X. Zeng, X. Fu, Y. Hu, Expandable microsphere-based triboelectric nanogenerators as ultrasensitive pressure sensors for respiratory and pulse monitoring, Nano Energy 59 (2019) 295–301, https://doi.org/10.1016/j.nanoen.2019.02.057.

[30] S. Chen, N. Wu, L. Ma, S. Lin, F. Yuan, Z. Xu, W. Li, B. Wang, J. Zhou, Noncontact heartbeat and respiration monitoring based on a hollow microstructured self-powered pressure sensor, ACS Appl. Mater. Interfaces 10 (4) (2018) 3660–3667, https://doi.org/10.1021/acsami.7b17723.

[31] Z. Zhou, S. Padgett, Z. Cai, G. Conta, Y. Wu, Q. He, S. Zhang, C. Sun, J. Liu, E. Fan, K. Meng, Z. Lin, C. Uy, J. Yang, J. Chen, Single-layered ultra-soft washable smart textiles for all-around ballistocardiograph, respiration, and posture monitoring during sleep, Biosens. Bioelectron. 155 (2020), 112064, https://doi.org/10.1016/j.bios.2020.112064.

[32] J. Liu, T. Jiang, X. Li, Z.L. Wang, Triboelectric filtering for air purification, Nanotechnology 30 (29) (2019), 292001, https://doi.org/10.1088/1361-6528/ab0e34.

[33] G. Liu, J. Nie, C. Han, T. Jiang, Z. Yang, Y. Pang, L. Xu, T. Guo, T. Bu, C. Zhang, Z.L. Wang, Self-powered electrostatic adsorption face mask based on a triboelectric nanogenerator, ACS Appl. Mater. Interfaces 10 (8) (2018) 7126–7133, https://doi.org/10.1021/acsami.7b18732.

[34] B. Ghatak, S. Banerjee, S.B. Ali, R. Bandyopadhyay, N. Das, D. Mandal, B. Tudu, Design of a self-powered triboelectric face mask, Nano Energy 79 (2021), 105387, https://doi.org/10.1016/j.nanoen.2020.105387.

[35] G.Q. Gu, C.B. Han, C.X. Lu, C. He, T. Jiang, Z.L. Gao, C.J. Li, Z.L. Wang, Triboelectric nanogenerator enhanced nanofiber air filters for efficient particulate matter removal, ACS Nano 11 (6) (2017) 6211–6217, https://doi.org/10.1021/acsnano.7b02321.

[36] C. Han, T. Jiang, C. Zhang, X. Li, C. Zhang, X. Cao, Z. Wang, Removal of particulate matter emissions from a vehicle using a self-powered triboelectric filter, ACS Nano 9 (23) (2015) 12552–12561, https://doi.org/10.1021/acsnano.5b06327.

[37] Y. Bai, C.B. Han, C. He, G.Q. Gu, J.H. Nie, J.J. Shao, T.X. Xiao, C.R. Deng, Z.L. Wang, Washable multilayer triboelectric air filter for efficient particulate matter PM2.5 removal, Adv. Funct. Mater. 28 (15) (2018), 1706680, https://doi.org/10.1002/adfm.201706680.

[38] C.M. Wu, M.H. Chou, Acoustic–electric conversion and piezoelectric properties of electrospun polyvinylidene fluoride/silver nanofibrous membranes, Express Polym. Lett. 14 (2) (2020) 103–114, https://doi.org/10.3144/expresspolymlett.2020.10.

[39] W. Wang, Y. Zheng, X. Jin, Y. Sun, B. Lu, H. Wang, J. Fang, H. Shao, T. Lin, Unexpectedly high piezoelectricity of electrospun polyacrylonitrile nanofiber membranes, Nano Energy 56 (2019) 588–594, https://doi.org/10.1016/j.nanoen.2018.11.082.

[40] Z. Li, J. Shen, I. Abdalla, J. Yu, B. Ding, Nanofibrous membrane constructed wearable triboelectric nanogenerator for high performance biomechanical energy harvesting, Nano Energy 36 (2017) 341–348, https://doi.org/10.1016/j.nanoen.2017.04.035.

[41] J. Shen, Z. Li, J. Yu, B. Ding, Humidity-resisting triboelectric nanogenerator for high performance biomechanical energy harvesting, Nano Energy 40 (2017) 282–288, https://doi.org/10.1016/j.nanoen.2017.08.035.

[42] B.U. Ye, B.J. Kim, J. Ryu, J.Y. Lee, J.M. Baik, K. Hong, Electrospun ion gel nanofibers for flexible triboelectric nanogenerator: electrochemical effect on output power, Nanoscale 7 (39) (2015) 16189–16194, https://doi.org/10.1039/c5nr02602d.

[43] F. Chen, Y. Wu, Z. Ding, X. Xia, S. Li, H. Zheng, C. Diao, G. Yue, Y. Zi, A novel triboelectric nanogenerator based on electrospun polyvinylidene fluoride nanofibers for effective acoustic energy harvesting and self-powered

multifocal sensing, Nano Energy 56 (2019) 241–251, https://doi.org/10.1016/j.nanoen.2018.11.041.

[44] Z. Qin, Y. Yin, W. Zhang, C. Li, K. Pan, Wearable and stretchable triboelectric nanogenerator based on crumpled nanofibrous membranes, ACS Appl. Mater. Interfaces 11 (13) (2019) 12452–12459, https://doi.org/10.1021/acsami.8b21487.

[45] H. He, M. Gao, B. Illés, K. Molnar, 3D printed and electrospun, transparent, hierarchical polylactic acid mask nanoporous filter, Int. J. Bioprint 6 (4) (2020) 278, https://doi.org/10.18063/ijb.v6i4.278.

[46] G.H. Zhang, Q.H. Zhu, L. Zhang, F. Yong, Z. Zhang, S.L. Wang, Y. Wang, L. He, G. H. Tao, High-performance particulate matter including nanoscale particle removal by a self-powered air filter, Nat. Commun. 11 (1) (2020) 1653, https://doi.org/10.1038/s41467-020-15502-7.

[47] Z. Zhang, D. Ji, H. He, S. Ramakrishna, Electrospun ultrafine fibers for advanced face masks, Mater. Sci. Eng. R. Rep. 143 (2021), 100594, https://doi.org/10.1016/j.mser.2020.100594.

[48] S. Motamedi-Fakhr, R. Iles, A. Barney, W. de Boer, J. Conlon, A. Khalid, R. C. Wilson, Evaluation of the agreement of tidal breathing parameters measured simultaneously using pneumotachography and structured light plethysmography, Physiol. Rep. 5 (3) (2017), e13124, https://doi.org/10.14814/phy2.13124.

[49] R.L. Colasanti, M.J. Morris, R.G. Madgwick, L. Sutton, E.M. Williams, Analysis of tidal breathing profiles in cystic fibrosis and COPD, Chest 125 (2004) 901–908, https://doi.org/10.1378/chest.125.3.901.

[50] S. Leonhardt, P. Ahrens, V. Kecman, Analysis of tidal breathing flow volume loops for automated lung-function diagnosis in infants, IEEE Trans. Biomed. Eng. 57 (8) (2010) 1945–1953, https://doi.org/10.1109/TBME.2010.2046168.

[51] W. Yang, X. Wang, H. Li, J. Wu, Y. Hu, Z. Li, H. Liu, Fundamental research on the effective contact area of micro-/nano-textured surface in triboelectric nanogenerator, Nano Energy 57 (2019) 41–47, https://doi.org/10.1016/j.nanoen.2018.12.029.

[52] J. Jamari, Kartini, E. Saputra, R. Ismail, J. Jamari, A.P. Bayuseno, R. Handogo, E. Suryani, Analysis of the contact area of smooth and rough surfaces in contact with sphere indenter using finite element method, MATEC Web Conf. (2016), https://doi.org/10.1051/matecconf/20165804007.

[53] S. Zhang, H. Liu, F. Zuo, X. Yin, J. Yu, B. Ding, A controlled design of ripple-like polyamide-6 nanofiber/nets membrane for high-efficiency air filter, Small 13 (10) (2017), https://doi.org/10.1002/smll.201603151.

[54] D.Y. Choi, S.H. Jung, D.K. Song, E.J. An, D. Park, T.O. Kim, J.H. Jung, H.M. Lee, Al-coated conductive fibrous filter with low pressure drop for efficient electrostatic capture of ultrafine particulate pollutants, ACS Appl. Mater. Interfaces 9 (19) (2017) 16495–16504, https://doi.org/10.1021/acsami.7b03047.

Haijun He is currently a Ph.D. candidate at the Department of Polymer Engineering, Budapest University of Technology and Economics in Hungary. He obtained his B.Sc. and M.Sc. degree in Textile Engineering and Textile Materials at Xi'an Polytechnic University (China) in 2014 and 2017, respectively. He started his Ph.D. study with the Stipendium Hungaricum Scholarship funded by the Tempus Public Foundation (Hungary) and China Scholarship Council (China) in 2017. His research interests are the development of new electrospinning methods for the scale-up of the nanofiber productivity, polymeric composites reinforced with nanofibers, 3D printing, and smart/functional nanomaterials.

Jian Guo is currently pursuing his Ph.D. in Electrical Engineering at the Budapest University of Technology and Economics. He also received his M.Sc. in Electrical Engineering at the Budapest University of Technology and Economics (2018). His doctoral research is on the development and implementation of multi-agent control algorithms in artificial intelligence field, such as game theory and reinforcement learning algorithms for multi-agent systems.

Balázs Illés is a full professor at the Budapest University of Technology and Economics and the head of the Department of Electronics Technology. He received the M.Sc. degree (in 2005), the Ph.D. degree (in 2009), and the dr. habil. degree (2015) in electrical engineering from Budapest University of Technology and Economics. In 2019 he was awarded the doctoral degree of the Hungarian Academy of Science. He has been involved in applied thermal sciences, heat and mass transfer, metallurgy in electronics assembling technologies, and the reliability of electronic equipment.
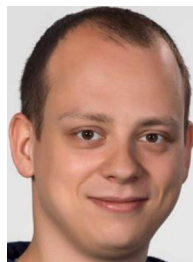
Attila Géczy is an associate professor at the Department of Electronics Technology, Faculty of Electronical Engineering and Informatics, Budapest University of Technology and Economics. He is a member of Hungarian Academy of Sciences Committee on Electronic Devices and Technologies. He is the president of the IMAPS Hungary Chapter. He was awarded the János Bolyai Scholarship, and he is the leader of the OTKA NKFI-FK-132186 project. His research interests are ranging from reflow technologies in electronics, biodegradables in electronics and applied sensors.

Balázs Istók is an assistant professor at the Department of Fluid Mechanics, Faculty of Mechanical Engineering, Budapest University of Technology and Economics (Hungary). In his Ph. D. thesis, he investigated the environmental emission of combined sewer systems using numerical modelling and field measurements. He participated in about 100 research or industrial consultancy projects in several application fields, such as atmospheric flows, gravitational flows, hydraulics, pipe transients and wind tunnel measurements. His research interests include LDA, PIV, concentration measurements in wind tunnels, modelling and measuring gravitational flow, building, and testing measuring systems.

Viktor Hliva obtained his B.Sc. and M.Sc. degree in Mechanical Engineering at the Budapest University of Technology and Economics (Hungary) in 2014 and 2017, respectively. He is currently a Ph.D. student at the Department of Polymer Engineering, Budapest University of Technology and Economics. His research interests are in the development of nondestructive test methods for polymer composites, digital image correlation, and 3D printing.

Dániel Török is an assistant professor at the Department of Polymer Engineering, Faculty of Mechanical Engineering, Budapest University of Technology and Economics (Hungary), and a research fellow at MTA-BME Lendület Lightweight Polymer Composites Research Group, Hungarian Academy of Sciences (Hungary). His research interests include injection molding, polymer testing, and polymer materials science.

József Gábor Kovács is an associate professor at the Department of Polymer Engineering, Faculty of Mechanical Engineering, Budapest University of Technology and Economics (Hungary), and a group leader of the MTA-BME Lendület Lightweight Polymer Composites Research Group, Hungarian Academy of Sciences (Hungary). He received several national awards, like the Hungarian Cross of Merit (2016, civil division), Bolyai János Research Scholarship (2008–2011 and 2012–2015, Hungarian Academy of Sciences), amongst many others. His research interests include injection molding and related technologies (e.g., T-RTM), polymer materials science, and simulations.

Kolos Molnár is an associate professor at the Department of Polymer Engineering, Faculty of Mechanical Engineering, Budapest University of Technology and Economics (Hungary), and a research fellow at the MTA-BME Research Group for Composite Science and Technology. He was appointed as professor extraordinaire at the Tshwane University of Technology (Pretoria, South Africa) in 2019. He was awarded the Youth Academy Award of the Hungarian Academy of Sciences in 2020 and the János Bolyai Scholarship in 2019. His research interests include the development of electrospun nanofibers and high throughput nanofiber technologies, nano- and self-reinforced composites, polymer testing and polymer materials science.

István Harmati is an associate professor at the Budapest University of Technology and Economics, Hungary. He received his Ph.D. in 2004 and since then he has contributed to his research field in several roles. Some highlighted (but not limited) work is the following: Technical Program Chair ISMCR2020, Program Committee member for IEEE International Conference on Model and Methods in Automation and Robotics (2002–2011), Member of IEEE, IEEE Robotics and Automation Society, Control Systems Society (2002–2011), Associate Editor of International Journal of Advanced Robotic Systems (2016-), regular reviewer for distinguished journals and several conferences.